PCCP

PAPER

View Article Online
View Journal | View Issue

Cite this: *Phys. Chem. Chem. Phys.*, 2014, **16**, 24443

Phonon modes of MgB_2: super-lattice structures and spectral response

Jose A. Alarco,*[ab] Alison Chou,[ab] Peter C. Talbot[ab] and Ian D. R. Mackinnon[a]

Received 2nd August 2014,
Accepted 18th September 2014

DOI: 10.1039/c4cp03449j

www.rsc.org/pccp

Micrometre-sized MgB_2 crystals of varying quality, synthesized at low temperature and autogenous pressure, are compared using a combination of Raman and infra-red (IR) spectroscopy. These data, which include new peak positions in both spectroscopies for high quality MgB_2, are interpreted using DFT calculations on phonon behaviour for symmetry-related structures. Raman and IR activity additional to that predicted by point group analyses of the *P6/mmm* symmetry are detected. These additional peaks, as well as the overall shapes of calculated phonon dispersion (PD) models are explained by assuming a double super-lattice, consistent with a lower symmetry structure for MgB_2. A 2× super-lattice in the *c*-direction allows a simple correlation of the pair breaking energy and the superconducting gap by activation of corresponding acoustic frequencies. A consistent physical interpretation of these spectra is obtained when the position of a phonon anomaly defines a super-lattice modulation in the *a*–*b* plane.

1. Introduction

Phonon properties of MgB_2 materials have been intensively investigated by optical techniques, such as Raman[1–15] and infra-red (IR)[16,17] spectroscopies, and are also complemented by experiments using inelastic X-ray scattering (IXS)[2,18–20] and inelastic neutron scattering (INS).[21–23] Derived phonon information extends to the electron–phonon interaction and superconducting energy gaps.[10,15,19,24] While these studies have described many properties of MgB_2, the spread of experimental results for phonon frequencies is wide and not always consistent. This inconsistency is likely due to variable quality of the investigated materials and to different data acquisition conditions. Anharmonicity,[1,2,18,22,23,25,26] phonon anomalies,[7,19,27] presence of impurities,[9,11,12,17] off stoichiometry from Mg deficiency,[19] defects,[19] or unreacted boron,[17] structural disorder or distortion[5,11,14–16] and multi-phonon contributions[16,20,25] are among the cited manifestations or reasons for divergent results on MgB_2 property–structure relations.

We have recently synthesized MgB_2 under conditions that result in a reproducible, dense and coarse-grained microstructure.[28] This coarse-grained MgB_2 has excellent electrical, magnetic and transport properties. By varying conditions of this synthesis process, we have also produced inferior quality MgB_2 which shows a lower superconducting transition temperature (T_c = 38.0 K) and lower density, finer-grained material.[28] This latter type of material is similar in form and property to that for which several spectroscopic observations on MgB_2 are reported.[5,13,15] This work examines differences in optical properties of two different forms of MgB_2, in order to evaluate potential causes for disparity of results in the current literature.[1,2,18–20,25–27]

Density functional theory (DFT) is used to estimate the phonon behaviour of MgB_2 based on well-determined crystallographic data using neutron and X-ray diffraction.[29–31] Point group analysis of the *P6/mmm* symmetry for MgB_2 predicts one Raman and two IR active peaks (see Table 4). However, other studies[1,2,8,15,32,33] as well as this one, suggest that additional Raman or IR active peaks are observed. *Ab initio* DFT has been used to calculate the phonon density of states (PDOS) and the phonon dispersion (PD) of MgB_2.[21,32,34–36] However, this literature also appears to show somewhat divergent results between computational models and experimental data.[1,32,34–36] In this work, experimental data are considered in light of modelling to estimate phonon frequencies, density of states and dispersion relations in MgB_2 with a particular focus on high quality MgB_2 crystals.

2. Methods

2.1 Experimental

Samples for this work are obtained by reaction of Mg metal and $NaBH_4$ precursors using a 50 ml Parr reactor as described by Mackinnon *et al.*[28] All materials are handled in a controlled atmosphere glove box containing Argon (99.99%). Starting materials are pre-heated in an evacuated chamber adjacent to the glove box in order to reduce to the dehydrated state and

[a] *Institute for Future Environments, Queensland University of Technology, 2 George St., Brisbane, QLD, 4001 Australia. E-mail: jose.alarco@qut.edu.au*
[b] *Science and Engineering Faculty, Queensland University of Technology, 2 George St., Brisbane, QLD, 4001 Australia*

then transferred to an inert atmosphere. Water and oxygen content in the glove box is normally less than 1 ppm. After MgB_2 is produced *via* this low temperature, autogenous pressure method,[28] the reaction chamber is cooled to room temperature and opened in the argon-filled glove box *via* slow pressure equilibration using a gas release valve. In general, material removed from the reaction chamber is placed immediately on substrates or contained within controlled atmosphere environments for subsequent characterisation.

For these Raman experiments, the samples, while still in the glove box, are placed inside a gas-tight Teflon sample chamber fitted with an optical (glass) window for Raman measurements. For IR measurements, the samples are handled in a similar manner to reduce exposure to air at all times up to the initiation of data collection. We have evaluated samples degraded in air over long times (*e.g.* days) to confirm Raman and IR characteristics of these materials. Data reported in this work are for samples with minimal degradation. Two types of MgB_2 samples are produced by the reactions described by Mackinnon *et al.*[28] and a summary of essential characteristics is given in Table 1.

Raman spectra are collected with an inVia Renishaw Raman microscope using two different excitation wavelengths: (i) a near-IR diode laser operating at 785 nm or (ii) a He–Ne laser operating at 532 nm. The laser power at the sample is 20 mW for the 785 nm laser and 10 mW for the 532 nm laser, focussed into a spot size of $\sim$1 μm through a $\times$50 objective lens. Each Raman spectrum consists of 4 accumulations with a 20 s exposure per scan. Spectrum noise and background are corrected using the smoothing and baseline correction functions in the GRAMS software.[37]

Attenuated total reflectance (ATR) FTIR measurements are recorded with a Nicolet iS50 ATR-FTIR spectrophotometer internally purged with dry air. All measurements are performed at room temperature with the sample (exposed to air) in direct contact with a diamond ATR crystal. Data are collected over an accumulation of 8000 scans at a speed of 0.02 min per scan, energy step 0.428 cm^{-1} and resolution of 4 cm^{-1} over the range of 350–1800 cm^{-1}.

A Leica multi-focus, stereo optical microscope and a Zeiss Sigma variable pressure field emission SEM with Oxford instruments silicon drift detector (SDD) are used for microscopy observations and energy dispersive spectroscopy (EDS) elemental analysis. Samples are prepared for SEM/EDS by placing a thin layer of powder onto aluminium stubs with double-sided carbon tape. In general, samples are not coated with a conductive coating to avoid analytical interference(s).

Table 1 Characteristics of MgB_2 samples used in this study

Characteristics	Sample A	Sample B
Maximum temp. of reaction (°C)	500	500
Heating profile hold temp. (°C)	At 50 and 250	No hold
Superconducting temp., T_c (°C)	38.5	38.0
Particle size (μm)	40–80	5–10
Particle morphology	Euhedral hexagon or bipyramidal	Thin platelet discs
Dominant color (incident light)	Gold	Black/grey
Lustre	Bright	Dull

2.2 Modelling calculations

The CASTEP module of Materials Studio 7.0 provides the functionality to calculate vibrational and associated properties such as IR and Raman spectra for a wide range of materials.[38] Both linear response (also known as density functional perturbation theory, DFPT) and finite displacement (FD) methods are used in this work. Gradient-corrected exchange–correlation functionals are supported in linear response calculations, although the results may be less accurate than those obtained with local density approximation (LDA) and the computational cost is noticeably higher.[39]

Most calculations are completed using Materials Studio 7.0 *via* the Microsoft Windows mode of a 12 core Mac Pro Xeon 64 bit workstation. This workstation operates with an Intel chip and mimics up to 24 cores. When memory requirements exceed the capacity of this computer, calculations are undertaken *via* the high performance computing (HPC) facility at QUT using multiples of 16 cores. The optimum choice for calculations on the HPC facility is 64 cores.

Specific functionals and the acronyms used to describe functionals in these CASTEP calculations (*e.g.* LDA–CA–PZ or GGA–PBE) for a different, albeit cubic, structure are described by Alarco *et al.*[40] The DFPT method is implemented in CASTEP for norm conserving potentials (NCPs). On the other hand, FD methods, although in principle available for both NCPs and ultrasoft potentials (UPs) are more effective with UPs. Some FD calculations using NCPs are possible with coarse *k*-grids but use of a finer *k*-grid resulted in negative frequency values and difficulty with convergence.

For single cell calculations on MgB_2, the lattice parameters $a = b = 0.3085$ nm and $c = 0.3523$ nm have been used as input.[29–31] For super-lattice calculations, appropriate multiples of these parameters have been used. Fig. 1 shows a schematic of the reciprocal space lattice for *P*6/*mmm* symmetry of MgB_2 where the green and grey spheres represent Mg and B atoms, respectively. Super-lattice constructions of the MgB_2 cell used in this work are multiples along the *c*-axis direction that retain similar reciprocal space directions.

3. Experimental results

In order to validate spectral data for both Raman and IR, a range of experiments are undertaken on each sample type to

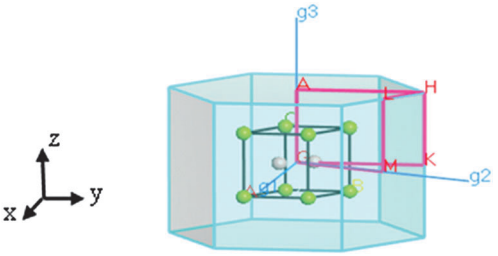

Fig. 1 Reciprocal space projection for the *P*6/*mmm* group that shows major symmetry directions. The real space primitive cell is also depicted.

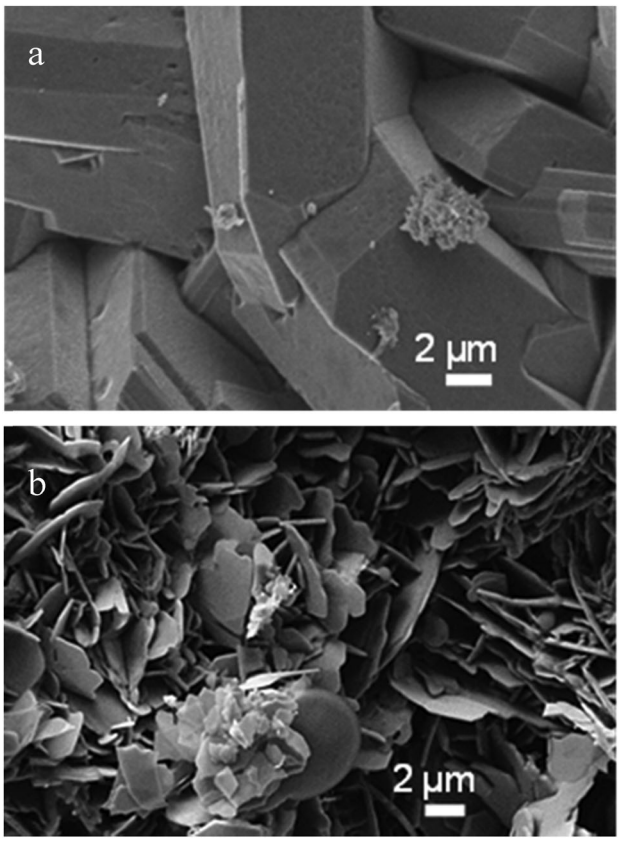

Fig. 2 SEM images of MgB_2 made by the same process with different operating parameters as shown in Table 1. (a) Sample A showing large euhedral crystal shapes approx. 40 μm to 60 μm and (b) Sample B showing smaller sized platy discs approx. 5 μm to 10 μm.

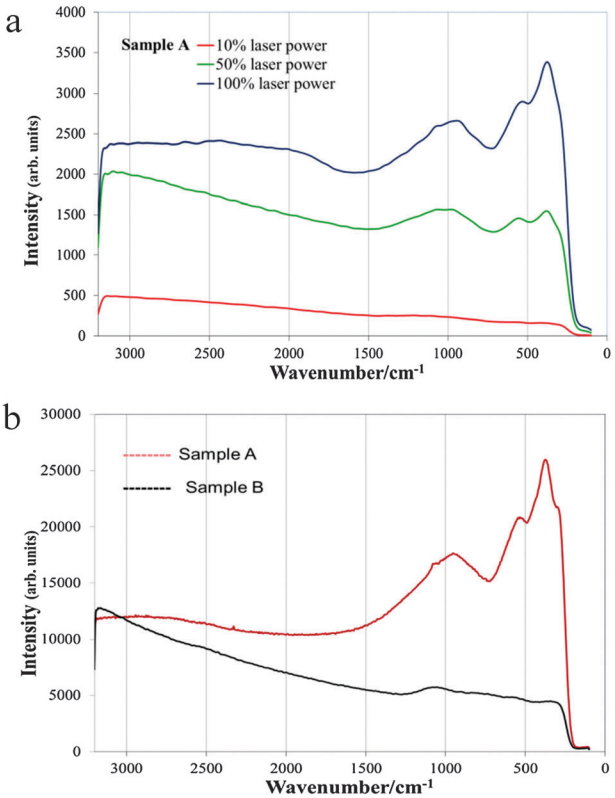

Fig. 3 Comparison of Raman spectra for: (a) Sample A with different percentage laser power; and (b) Samples A and B at 100% laser power (excitation laser 532 nm). Samples are exposed to air during the acquisition of spectra.

evaluate key parameters that influence interpretation. These experiments are aimed at evaluating the quality of spectra and dependence on, for example, power rating and illumination, wavelength, incident intensity, particle morphology and exposure to air. This *a priori* approach to Raman and IR spectra for MgB_2 is not apparent in the current literature albeit other phases have been evaluated.[41–43]

SEM images of Samples A and B are shown in Fig. 2. The difference in morphology between each sample is demonstrable albeit each sample shows a similar X-ray diffraction pattern for MgB_2.[28]

3.1 Raman acquisition parameters

Fig. 3a shows a comparison of the Raman spectra for Sample A acquired with varying laser power and exposed to air during the acquisition of spectra. The presence of peaks in the Raman spectrum is apparent when the percentage of laser power is greater than 10%. Peak definition is optimal for Sample A at 100% laser power or ~20 mW. Unlike some materials that, under high power conditions are often overheated or destroyed,[44–47] both samples appear unaffected in this manner.

Fig. 3b shows a comparison of Sample A and B under the same illuminating conditions. These spectra show that larger size grains enhance the observation of well-defined Raman peaks as noted in earlier work on different compounds by a number of authors.[41–43,47]

Fig. 4 shows an example of Raman spectra from Sample A acquired at 532 nm with freshly prepared material and minimum exposure to air. Notice the peak at ~230 cm^{-1}, which is close to peaks observed and calculated in other Raman studies of MgB_2.[2,11,32,34] Additional Raman peaks (labelled with "*") are also observed in Fig. 4b, presumably due to different orientations of these larger size grains. Minor amplitude variations due to instrument noise are also observed in Fig. 4b (arrowed).

Fig. 5 shows Raman spectra for Sample A collected on different days, at two laser excitations. The spectra show a close match of peak positions at low wavenumbers. Up to nineteen Raman active peaks as compiled in Table 2 can be identified in the spectra collected on this high quality sample of MgB_2.

Table 2 gives a summary of the peak positions detected in the Raman spectra from Sample A as shown in Fig. 3–5. Inspection of data in Table 2 shows that some frequencies – within experimental error – are grouped together or are common to both illumination wavelengths. Minor differences in explicit values may be attributed to slightly different temperature effects. However, for experiments summarized in Table 2, low energy peaks consistently occur and occur repeatedly with comparable intensity and peak width. This occurrence implies that these low energy peaks are active to similar extent and are not governed by *P6/mmm* symmetry.

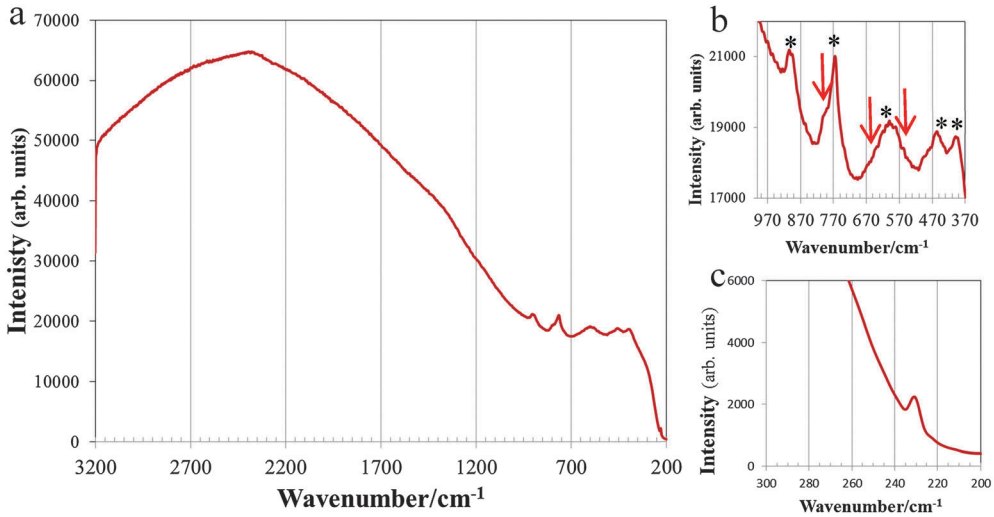

Fig. 4 Raman spectra from (a) fresh Sample A at excitation wavelength 532 nm. Figures (b) and (c) are expanded views of key regions from the spectrum in (a). Small amplitude variations in (b) are from instrumental noise (arrowed).

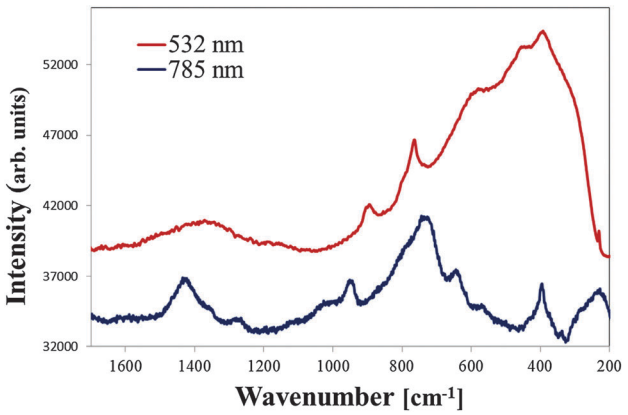

Fig. 5 Raman spectra from Sample A collected on different days at two illumination conditions.

3.2 Infra-red acquisition parameters

Samples for IR characterization are briefly exposed to air due to the configuration of the sample holder and diamond window. In this method, a reflection configuration provides a path that enhances the IR signal from the interior of a sample which extends the time period for acquisition before sample degradation dominates the spectrum. This technique, which increases the absorption path, reduces the influence of surface effects on IR spectra compared with Raman spectroscopy. Fig. 6 shows IR spectra from a freshly exposed piece of Sample A and from Sample B.

Table 3 lists the approximate peak positions of IR spectra for samples A and B. For sample A, peak parameters are determined by Gaussian peak-fitting routines with GRAMS software.[37] For sample B, peak positions are listed since Gaussian fits do not produce reasonable spectral shapes. This spectrum is also difficult to fit using combinations of Lorentzian and Gaussian peak shapes.

Table 2 Characteristics of Raman Spectra for Sample A

	Peak centre [cm^{-1}]			
Peak	From Fig. 3[a] 532 nm	From Fig. 4	From Fig. 5	From Fig. 5 785 nm
1		230	246	247
2	299		300[b]	297
3				353
4	382	393	397	398
5		406	406	
6		464	465	454
7	530–552			
8		603	590	594
9				657
10		767	767	749
11		803		800
12		908	906	
13	940–973			958
14				1047
15	1062–1073			
16				1295
17			1385	1378
18				1435
19		2433		

[a] Laser power at 50% produces slightly higher peak shift positions compared with 100% laser power. [b] This position is uncertain due to over-lapping intensity at a shoulder peak.

3.3 Modelling results

The presence of additional peaks that may not be described by *P6/mmm* symmetry in experimental data from both Raman and IR methods, suggests computational models may be used to provide higher accuracy and/or precision for interpretation. Thus, modelling in this work evaluates the reciprocal space *k*-grid and relevant grid intervals, the space group and lower symmetry conditions for MgB_2. Results from these modelling approaches are described below.

3.3.1 *k*-grid interval. The fineness of the *k*-grid is known to affect the accuracy and convergence of phonon calculations as demonstrated in a number of publications including an

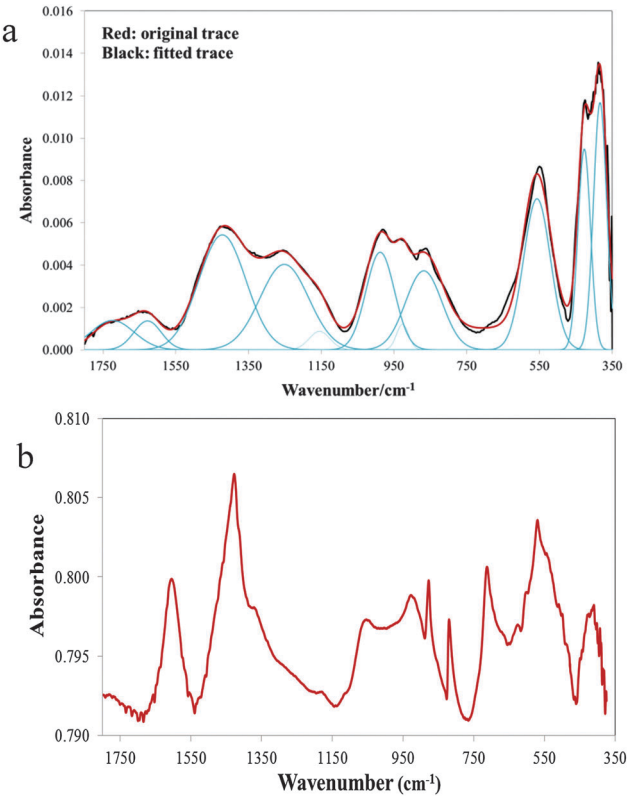

Fig. 6 IR spectra collected from freshly exposed (a) Sample A and (b) Sample B.

Table 3 Characteristics of IR Spectra for Samples A and B

Sample A					Sample B
Peak No.	Centre [cm^{-1}]	Height	Width [cm^{-1}]	Area	Centre [cm^{-1}]
1	384	0.0104	36	0.39	385, 394
2	425	0.0101	45	0.48	412, 427
3	557	0.0078	96	0.80	547, 570
4					628
5					820
6	868	0.0033	110	0.39	878
7	930	0.0017	48	0.09	928
8	990	0.0043	80	0.37	
9					1053
10	1190	0.0017	103	0.18	1183
11	1282	0.0033	156	0.55	
12					1369
13	1428	0.0047	136	0.69	1427
14	1632	0.0016	92	0.16	1604
15	1727	0.0016	114	0.18	
16					1804

excellent summary by Ackland *et al.*[39,48] A comparison of the phonon dispersion relations obtained by the linear response (or DFPT) method with decreasing interval of the *k*-grid is shown in Fig. 7. DFPT calculations converge satisfactorily when the materials are assumed as metal and calculations are with NCPs. The significance of the "metal" designation in Materials Studio calculations is described by Alarco *et al.*[40] Two functionals have been evaluated for this DFPT method – the LDA–CA–PZ and the GGA–PBE functional. In each case, the calculated outcomes are equivalent.

The region between 400 cm^{-1} and 650 cm^{-1} around the *G* (or *Γ*) point is a noteworthy feature (circled in Fig. 7) that varies considerably with change in *k*-grid interval. For Raman active frequencies, the region around the *G* direction shifts from a single degenerate "dip" at ~450 cm^{-1} at the *G* centre point to a degenerate "Mexican hat" configuration (with two adjacent dips) located between the *G*–*K* and *G*–*M* directions with decreasing grid interval. In addition, the doublet minima, or approximately degenerate bands, shift(s) to higher frequency at ~550 cm^{-1}.

Table 4 shows the values for Raman active frequencies as the interval of the grid is decreased. A substantial change from 425 cm^{-1} to the 550–650 cm^{-1} range occurs with decreasing *k*-grid interval. These frequencies span the range of values reported in the literature for MgB_2 under different experimental conditions as noted below.

Similar calculations have been attempted using the FD method, but convergence occurs only with use of UPs. For example, with a coarse *k*-grid at 0.07 A^{-1}, anomalous behaviour of the lower phonon bands occurs along the reciprocal space AH–HK and ML–LH directions. This anomalous behaviour becomes extreme (*i.e.* with negative values), when NCPs are used with either LDA–CA–PZ or GGA–PBE functionals. However, calculations using UPs eliminate these lower band anomalies in most cases. A strong peak at a very high frequency (~890–910 cm^{-1}) for the Raman active mode at the *Γ* (or *G*) point is maintained at fine grid scale.

Additional calculations with the FD method show that the lowest acoustic band tends to deviate from other acoustic bands when using the GGA–PBE functional and is less pronounced for the LDA–CA–PZ functional. This relative difference occurs for fine *k*-grids of 0.02 A^{-1} and is shown in Fig. 8 as PD plots. However, the peaked Raman active mode reverses shape to form a "valley" near the *G* point. This form of the Raman active mode is similar to that determined from DFPT methods with corresponding calculated frequency values closer to experimental values (compare Fig. 7 and 8). Optimum results for the FD method are obtained with this *k*-grid interval and a super-cell cut-off radius of 5 A.

Calculations using a larger cut-off radius and/or a finer *k*-grid to improve accuracy led to unviable, extremely long calculation times. These calculations are terminated once the pre-set time limit between three and five days is achieved without iteration progress.

3.3.2 Lower symmetry models. Table 5 shows a comparison of active and inactive modes for the space group *P*6/*mmm* with other related lower symmetry groups that contain symmetry elements of the parent space group. While the actual frequencies remain near constant, for lower symmetry the Raman and IR active peaks are significantly different. For example, the 413.3 to 416.9 mode is Raman active for *P*6 and *P*6*mm* symmetries but not for all other symmetries listed in Table 5. Note that in some cases, the mutual exclusion rule for IR and Raman active modes in centrosymmetric groups is not upheld.[49–51]

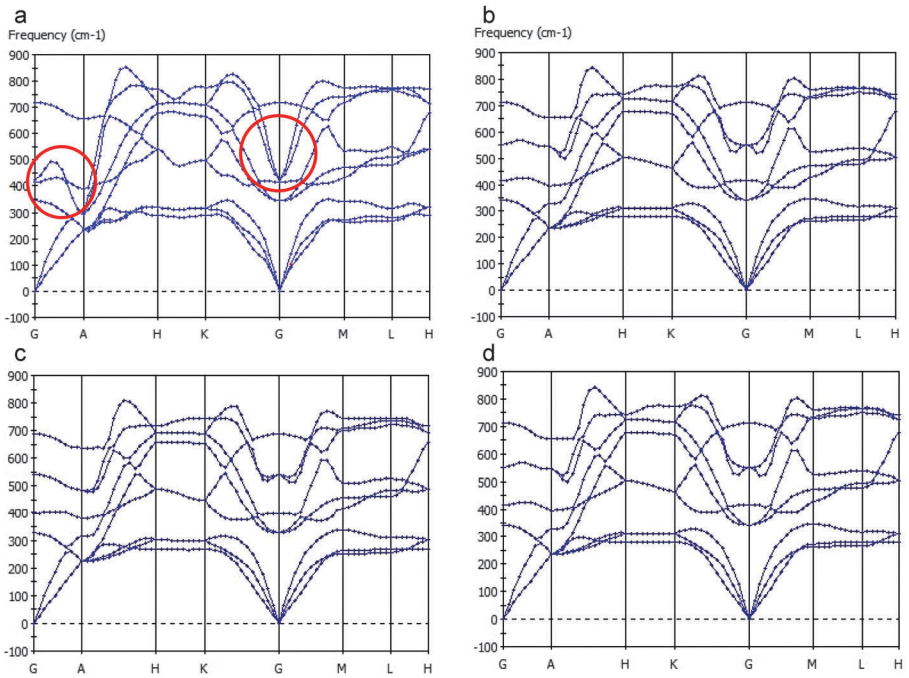

Fig. 7 Phonon dispersion (PD) calculations for group *P6/mmm* using a linear response with increasing fineness (or decreasing interval) of *k*-grid: (a) k = 0.04 A^{-1}, (b) k = 0.03 A^{-1}, (c) k = 0.02 A^{-1}, (d) k = 0.015 A^{-1}.

Table 4 MgB_2 Raman active frequencies for *P6/mmm* symmetry

Minimum **k**-vector [A^{-1}]	Raman active mode [cm^{-1}]
0.04	425.89
0.03	644.61
0.02	582.29
0.015	551.04

3.3.3 Super-lattice structures. The use of superstructure modes to address the vibrational properties of MgB_2 is discussed by Tschauner *et al.*[52] For example, a doubling of the *c* axis parameter for MgB_2 and in space group $P6_3mc$ allows for two Raman active modes, while space group $P\bar{3}c1$ allows for three modes, $P\bar{6}c2$ allows for six and $P6_3cm$ allows for eight Raman active modes.[52] In space group *P3c*1, nine modes are both Raman and IR active.[52]

In this work, examples of lower symmetry which cannot be represented in a single unit cell have also been explored. Thus, to achieve the distribution of atoms, we have used super-lattice structures that reproduce the spatial arrangement of Mg and B atoms in the basic MgB_2 structure.[29–31] For the double super-lattice construction in the *c*-direction to represent the primitive cell, a lower symmetry and separate insertion of two B atoms is required. This construct is not necessary for the higher *P6/mmm* symmetry, where inserting one B atom replicates all the other B atom positions. Thus, in this format where B atoms are linked by different symmetry elements compared to the basic *P6/mmm* symmetry of MgB_2,[29–31] movement of adjacent B atoms is less constrained in order to conserve symmetry. A similar situation can be envisaged for Mg atoms under an appropriate choice of reduced symmetry as shown for $P\bar{3}c1$

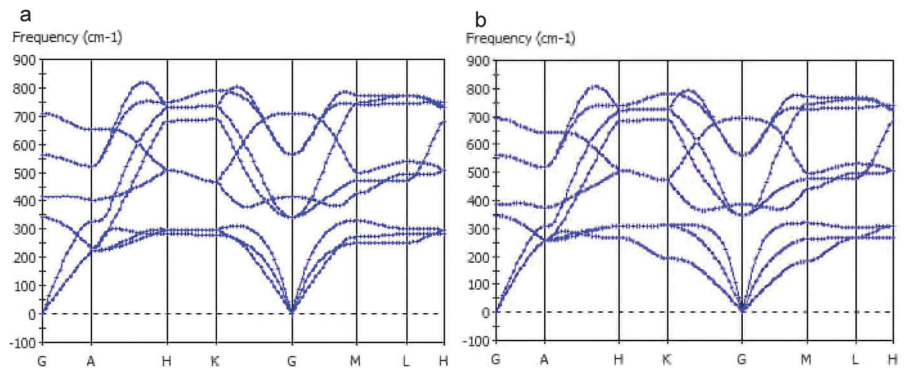

Fig. 8 Phonon dispersion (PD) for space group *P6/mmm* calculated with the FD method using k = 0.02 A^{-1} and a super-cell cutoff radius 5 A for (a) LDA–CA–PZ functional and (b) GGA–PBE functional.

Table 5 Active and inactive modes for *P*6/*mmm* and related lower symmetries

	Group													
	*P*6 168[b]		*P*$\bar{6}$ 174[b]		*P*6/*m* 175[b]		*P*622 177[b]		*P*6*mm* 183[b]		*P*$\bar{6}$*m*2 187[b]		*P*6/*mmm* 191[b]	
Frequency (cm^{-1})	IR	R	IR	R	IR	R	IR	R	IR	R	IR	R	IR	R
342.8–344.3 (dd)	Y	Y	Y	Y	Y	N	Y	Y	Y	Y	Y	Y	Y	N
413.3–416.9	Y	Y	Y	N	Y	N	Y	N	Y	Y	Y	N	Y	N
425.9–644.7[a] (dd)	N	Y	Y	Y	N	Y	N	Y	N	Y	Y	Y	N	Y
711.6–716.9	N	N	Y	N	N	N	N	N	N	N	Y	N	N	N

[a] These values display strong dependence on the dimension of the *k*-grid. Other frequencies display smaller variations (<6 cm^{-1}) that are largely attributable to minor differences in lattice parameters calculated during geometry optimization. (dd) indicates a doubly degenerate mode. [b] Value is the space group number.

Table 6 Calculated frequencies and active/inactive modes for super-lattice groups with reduced symmetry

	Group							
	*P*3*c*1 158[b]		*P*$\bar{3}$*c*1 165[b]		*P*$\bar{6}$*c*2 188[b]		*P*6$_3$*mc* 186[b]	
Frequency (cm^{-1})	IR	R	IR	R	IR	R	IR	R
233.4 (dd)	Y	Y	Y	N	N	Y	N	Y
237.4 (dd)	Y	Y	N	Y	Y	Y	N	Y
336.4	N	N	N	N	N	N	N	N
343.0 (dd)	Y	Y	Y	N	Y	Y	Y	Y
395.4	N	N	N	N	N	N	N	N
415.9	Y	Y	Y	N	Y	N	Y	Y
534.9 (dd)	Y	Y	Y	N	Y	Y	Y	Y
426.1–580.8[a] (dd)	Y	Y	N	Y	Y	Y	N	Y
657.0	N	N	N	N	N	N	Y	Y
712.4	Y	Y	N	Y	Y	N	N	N

[a] These values display strong *k*-grid dependence with minor differences attributable to lattice parameter geometry optimization. (dd) indicates a doubly degenerate mode. [b] Value is the space group number.

and can be constructed for the other forms of lower symmetry described in this work.

Fig. 9 shows the PD as a function of decreasing interval of *k*-grid for the lower group symmetry *P*$\bar{3}$*c*1. The broad features of the PD for *P*6/*mmm* symmetry as shown in Fig. 7 and 8 are largely maintained albeit a higher band population along similar reciprocal directions appears. The ''Mexican hat'' form of the near degenerate bands in the region 500–600 cm^{-1} still remains. At the smaller *k*-grid interval (Fig. 9b), an additional band at $\sim$650 cm^{-1} occurs but is not bifurcated nor a doublet. Fig. 9b also shows that the optical and acoustic bands are in closer proximity compared with Fig. 9a at higher *k*-grid interval. As expected, along the super-lattice ΓA line direction, substantial creation of new branches and/or breaking of degeneracy can be observed as a result of the folding of the Brillouin zone (in similar fashion to illustrations in Fig. 17 (ref. 42)).

Table 6 shows the frequencies and respective IR and Raman active modes for the lower symmetry super-lattices determined by these PD calculations. The majority of frequencies that correspond to symmetry *P*6/*mmm* are reproduced. Remarkably, additional frequencies between 230 cm^{-1} and 240 cm^{-1} occur. These frequencies are similar to values determined by the experimental measurements noted above. Additional higher frequencies also occur and appear similar to experimentally observed frequencies.

4. Discussion

Experimental Raman results from this work show that MgB_2 spectra are sensitive to acquisition and sample condition such as the grain size of the material as well as the energy and power of laser excitation (see Fig. 3). This sensitivity is consistent with prior reports on grain size dependence of Raman peak shapes[41–43,47] and partly explains the disparity of Raman results in the literature, as many characterized materials are fine grained. Few large crystals have been analyzed, and of those, primarily along high symmetry orientations.[2,5,9,10,20] In other cases, the presence of impurities may influence the quality of observed spectra. For example, in the work by Rafailov *et al.*[11] MgB_2 formed in a quartz ampoule at 900 °C from Mg powder and B powder shows a grain size of about 45 nm in diameter.[11] However, the presence of MgO impurity is indicative of a potential interaction with the quartz tube. Thus, Raman data from this work[11] may be difficult to interpret due to impure composition and very fine particle size.

To place this study into perspective, we summarize below prior publications on Raman and IR spectroscopy of MgB_2, in conjunction with prior modelling of MgB_2 phonon behaviour.

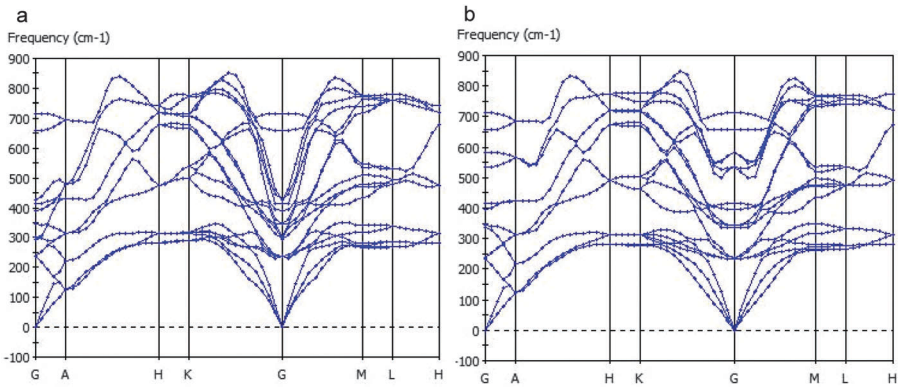

Fig. 9 Phonon dispersion (PD) for group *P*$\bar{3}$c1 calculated with increasing fineness of *k*-grid: (a) k = 0.04 A^{-1}, (b) k = 0.02 A^{-1}.

A consistent interpretation of these data through model and experiment is possible with an evaluation of symmetry conditions for the MgB_2 structure.

4.1 Prior spectroscopy

4.1.1 Raman properties. The general consensus is that MgB_2 belongs to space group $P6/mmm$ (D_{6h}), as determined from refinements of X-ray and neutron diffraction data.[29–31] For this space group, factor-group analysis predicts four modes at the Γ point: E_{1u}, A_{2u}, E_{2g} and B_{1g}, where only the E_{2g} mode is Raman-active, the E_{1u} and A_{2u} modes are IR active, and the B_{1g} mode is silent.[1,7] According to Quilty,[10] MgB_2 belongs to the D_{6h} point group, with Raman-active symmetry species A_{1g}, E_{1g} and E_{2g}, which appear to include Raman activity of the A_{1g} and E_{1g} modes at the A point.[1] The E_{2g} Raman-active phonon mode is doubly degenerate at Γ and involves in-plane, anti-phase stretching and hexagon-distorting displacements of the B atoms.[7,22,25,53] Kunc *et al.*[1] have shown the decomposition of the coordinate representation and the phonon displacement patterns at both Γ and A. The branch $E_{2g}(\Gamma)$–$E_{2u}(A)$ in the phonon dispersion exhibits the strongest electron–phonon coupling,[1,18,25,34,54] and $B_{1g}(\Gamma)$ is the z-displacement analogue of $E_{2g}(\Gamma)$.[1]

While most Raman experiments detect the frequency $\sim$75 meV (= 604.9 cm^{-1}), which corresponds to the E_{2g} mode, measurements also identify peaks with magnitude and temperature dependence that appear closely related to the pair breaking energy or superconducting gap.[1,6,9,10,24,55] For example, upon cooling of an MgB_2 sample below 50 K, Kunc *et al.*[1] have observed a build-up of additional scattering intensity in the range 50–300 cm^{-1} (Fig. 8(a) of ref. 1). This additional intensity can be modeled by two Gaussian peaks located at 128 and 226 cm^{-1}, respectively, in the 2 K spectrum.[1] These peaks are observed only for parallel polarizations of the incident and scattered light. With increasing temperature, these peaks vanish at a temperature between 74 K and 100 K; values that are well above T_c.[1]

Additional peaks are also observed in other Raman studies.[5,9,11] These additional peaks are not attributable to the E_{2g} mode nor to the pair breaking energy mentioned above and have not received much attention in the literature. These additional peaks are of weak magnitude and do not appear to show strong electron–phonon coupling. In addition, the conditions for detection of these weak peaks are limited, easy to confuse and readily attributed to an artifact. For example, Hlinka *et al.*[5] have observed humps in Raman spectra of large crystals from thick films at about 300 cm^{-1}, 400 cm^{-1}, 600 cm^{-1}, 750 cm^{-1} and 830 cm^{-1}. These values correspond approximately to the reported peaks for PDOS computed in this study and documented above. Rafailov *et al.*[11] investigated the Raman spectra of MgB_2 and systematically compared the data with potential impurities. In their work,[11] peaks at 250 cm^{-1}, 600 cm^{-1} and 750 cm^{-1} are assigned to MgB_2. However, in the same study, peaks at 255 cm^{-1}, 517 cm^{-1}, 1370 cm^{-1} and 1590 cm^{-1}, and another set at 380 cm^{-1}, 560 cm^{-1} and 960 cm^{-1} are measured as the light and dark areas (which we interpret to represent Mg and MgO), respectively, of an unreacted Mg stripe.[11]

4.1.2 IR properties. IR spectroscopy studies on MgB_2 are not as abundant as Raman spectroscopy experiments. Sundar *et al.*[16] measured the IR spectra of MgB_2 in the range of 125 cm^{-1} to 700 cm^{-1} as a function of temperature to 5 K. They found that the absorption spectrum is characterised by a broad band centered at 485 cm^{-1}, with shoulders at 333 cm^{-1} and 387 cm^{-1}. Additional further sharp features are observed at 542 cm^{-1}, 592 cm^{-1} and 633 cm^{-1}, which appear to match modes of β-rhombohedral boron. These features are attributed to the activation of boron-like modes in MgB_2 by disorder. Other high frequency modes manifested as broad bands centered at 1040 cm^{-1}, 1442 cm^{-1} and 1635 cm^{-1} appear to be a multiple of the absorption band at 485 cm^{-1} and hence, may be due to a combination of modes.[16] In a subsequent publication,[17] the small features at 333 cm^{-1}, 387 cm^{-1}, 542 cm^{-1}, 592 cm^{-1} and 634 cm^{-1} are associated with small amounts of unreacted B, as can be inferred from comparison with the spectrum for crystalline B.

4.2 Prior computational modelling of phonons

Ab initio DFT has previously been used to calculate the PDOS and the PD of MgB_2.[21,32,34–36] Kong *et al.*[34] use the linear-response, full-potential, Linear-Muffin-Tin-Orbital (LMTO) DFT method, developed earlier by Savrasov.[56,57] Shukla *et al.*[32] use DFT GGA with NCPs and linear response to compute harmonic frequencies and to determine a theoretical PD that matches their experimental data from IXS. Bohnen *et al.*[35] calculate the PD of MgB_2 to compare with that of isostructural AlB_2, using a mixed-basis pseudopotential method. This mixed pseudopotential model is a linear response approach similar to that of Kong *et al.*[34] Osborn *et al.*[21] have used a simple Born–von Karman (BvK) model for the PDOS to represent the main peaks in their INS experiments. Other works, which limit the calculation to phonon frequency shifts, often use the frozen phonon approach.[1,26,54] This approach is only valid when coupling between different modes is negligible and anharmonic interaction does not change significantly over the Brillouin zone.[26]

According to Parlinski,[36] far from the Γ-point, the acoustic PD relations reflect the vibrations of the Mg atoms in MgB_2. The optic branches describe vibrations of the graphite-like boron network. Moreover, the branches of symmetry A_{2u} and B_{1g} at the Γ-point correspond to the out-of-plane boron vibrations, while four remaining curves with symmetry E_{1u} and E_{2g} at the Γ-point determine the in-plane boron motion. The out-of-plane and in-plane polarizations are approximately along the same branches all over the Brillouin zone.[36]

For reference, Fig. 10 shows the directions of vibration for boron atoms in the MgB_2 structure defined by the E_{2g} mode. A dynamic description of vibration modes for MgB_2 is given by Yildirim.[53]

4.3 Spectral data – symmetry implications

Our experimental results from both Raman and IR spectroscopy as described above indicate that a higher number of

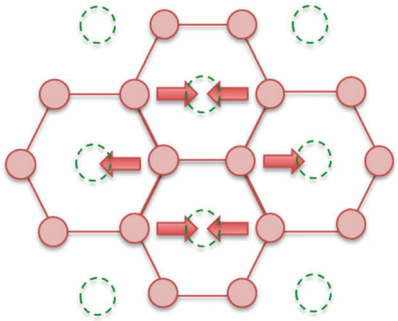

Fig. 10 Schematic showing directions of E_{2g} vibrations (arrows) for boron atoms in MgB_2. The dotted circles represent locations of Mg atoms above and below the boron plane.

peaks than are predicted by group theory analysis for *P*6/*mmm* symmetry occur for Sample A. Conventional analysis for the *P*6/*mmm* space group predicts one Raman active mode and two IR active modes. In comparison, our data suggest at least seven modes are active in both Raman and IR spectra obtained from Sample A. In addition, some peak frequencies appear to be both Raman and IR active. Several reasons for this spectral response are examined below.

A random orientation of large grained, polycrystalline, materials and larger crystal faces of Sample A likely contribute to ready detection of additional peaks compared with Sample B albeit additional peaks are identified. The presence of extra peaks in Raman spectra of MgB_2 is not exclusive to this work alone (see Section 4.1.1). In addition, several peaks appear to be both Raman and IR active. This outcome indicates not only that the symmetry is reduced with respect to *P*6/*mmm*, but also that the reduced symmetry may be non-centrosymmetric. For centrosymmetric materials, the rule of mutual exclusion for Raman and IR spectra requires a peak to be either Raman or IR active.[49–51] However, this need not apply for non-centrosymmetric materials.

Earlier calculations of MgB_2 vibrational behaviour[26,54] demonstrate use of the frozen phonon approach. However, as mentioned by Kunc *et al.*,[1] the frozen-in displacements required to perform these calculations lower the rotational symmetry of the system from D_{6h} (or *P*6/*mmm*) to D_{3h}, among other possibilities. Our calculations with reduced symmetry soften the constraints on Raman and IR activity without significant change to the frequency values as shown in Table 5.

Quantitative determination of specific factors such as anharmonicity,[1,2,18,22,23,25,26] phonon anomalies,[7,19,27] presence of impurities[9,11,12,17] and multi-phonon contributions[16,20,25] on the perturbation of first order vibrational features of MgB_2 is outside the scope of this article. However, it is worth noting that the Raman spectra from these experiments show fluorescence in the 1000–4000 cm^{-1} range (see Fig. 3a). This fluorescence is likely to be related to the generation of second order vibrational features.[58]

Constructing a super-lattice to model structures with reduced symmetry appears to match earlier determinations of MgB_2 phonon dispersions.[21,32,34–36] However the match between model and experiment is reasonable only if we consider that the multiplicity or near degeneracy of certain bands is partly hidden by experimental errors, or limited resolution, of the data. For instance, the E_{1u} energy at the Γ point in Fig. 3 of the article by Shukla *et al.*[32] appears to be the same energy as the top region of the highest energy acoustic mode at the *M* point. This study (Fig. 6 and 8) shows that a super-lattice with reduced symmetry reproduces the experimental data of Shukla *et al.*[32] This alternative interpretation is informative, given that phonon dispersions in the work reported by Shukla *et al.*[32] are constructed to fit experimental data from IXS[2,18–20,32] and INS,[21–23] respectively.

Symmetry conditions may also influence the accuracy of computational models for MgB_2 spectra and the nature of Raman or IR activity. For example, experimental results and models more closely align when the 6-fold rotation axis is reduced to a 3-fold rotation axis, resulting in a doubling of the unit cell in the *z*-direction. This difference in symmetry description – which invokes a super-lattice in the *z* direction – predicts a higher number of Raman and IR active modes than with conventional six-fold symmetry. This outcome suggests that the Mg atoms have also lost 6-fold symmetry. The manifestation of this lower symmetry is an alternating Mg atom position towards and away from the plane containing boron atoms. Furthermore, the reduced symmetry super-lattice model predicts an additional frequency at about 235 cm^{-1}. This frequency is observed in a number of experiments including this work as shown in Table 2.

4.4 Comparison of DFPT and FD modelling methods

Within DFT, the calculation of lattice dynamics is, in essence, the change in electronic charge density induced by the presence of a phonon with wave vector **q**.[56] Within the framework of the linear-response (or DFPT) method, calculation of the phonon spectra and the electron–phonon interaction is reduced to finding the first-order variations in the one-electron wave functions, the charge density and the effective potential induced by the presence of a phonon with a given wave vector **q**.[57] In addition, the linear response method provides an analytical means to compute the second derivative of the total energy with respect to a given perturbation.

On the other hand, the FD method, as exemplified by the extension of the LMTO method described by Savrasov,[56] is an analytical version of a finite-difference approach within a super-lattice. When applied to the same problem, the results of both approaches, DFPT and FD, must be the same except for errors that may be introduced by taking finite differences.

As noted,[39] phonon spectra in metallic compounds are very sensitive to details of the Fermi surface. To obtain reasonable spectra using the linear response method for metals, the *k*-point sampling must be dense and significantly higher density than the Fine mesh setting in CASTEP.[39] Based on experience, we recommend setting the separation parameter on the *k*-points tab of the CASTEP electronic options dialog to less than 0.02 A^{-1}. A clear sign of insufficient quality of *k*-point sampling is the presence of imaginary acoustic modes near the Γ-point.

In these calculations, the pseudo potentials mimic how valence electrons experience the screened core potential.[59] In practice, agreement is expected between the integrated real and pseudo charge densities outside a chosen core radius for each valence state.[60] The norm conservation criteria essentially ensures that the total charge of each pseudo wave function equals the charge of the all-electron wave function potential.[59] For both DFPT and FD methods, changes in the E_{2g} region of the PD are accompanied by changes in the ΓA, ΓM and ΓK directions. However, these changes are more pronounced in different phonon branches.

The PD calculated from the DFPT model, when using a sufficiently dense grid ($k < 0.03$ A^{-1}) displays the typical "Mexican-hat" topology for the mode around E_{2g} as shown in Fig. 6. According to Kunc *et al.*,[1] this mode corresponds to vibrations in the boron plane. Such topology has been extensively discussed for systems displaying the Jahn–Teller (JT), or pseudo-Jahn–Teller effect[61–64] and may be a signature of this effect in the MgB_2 system. Moreover, calculations with LDA and GGA functionals result in identical PDs in DFPT, while LDA and GGA clearly differ in the FD approach. Apparently, the charge redistribution in the DFPT method, required with the charge renormalization for NCPs, is accounted for primarily by the "Mexican-hat" changes in the PDs. In comparison, charge re-distribution is not imposed to the same extent in the FD method and results in larger modifications of the PD in the acoustic band region.

4.5 Phonon anomalies

Phonon anomalies, primarily in acoustic branches, are associated with improvement in the superconducting transition temperature (T_c) of structurally related materials.[65] In the case of MgB_2, Wood *et al.*[27] argue for the existence of an acoustic phonon anomaly in the ΓA direction on the basis of DFT calculations. Their results[27] resemble the crossing of the second and third branches that are observed in PD calculations shown in Fig. 7 and 9.

Baron *et al.*[19,66] identify the anomaly of the E_{2g} mode as a Kohn anomaly,[67] which originates from partial screening of lattice vibrations by the conduction electrons. This screening changes rapidly on certain surfaces in the space of phonon **q**-vectors and therefore, on these surfaces the frequencies vary abruptly with **q**.[67]

Baron *et al.*[19] also report the presence of an anomalous optical mode in MgB_2, similar in energy to that of the E_{2g} mode, but with a different line width and symmetry. This mode is longitudinal along ΓA and not predicted by the theory used at the time. Remarkably, calculations of the PD shown in Fig. 9 (and listed in Table 6) for the double cell symmetry predict a flat branch at $\sim$650 cm^{-1}, which is similar to values associated with the E_{2g} mode.

4.6 Reduced symmetry dynamics

The inference from these calculations that adjacent Mg atoms may move out of phase for a 3-fold reduced symmetry indicates that Mg atoms may also respond to in-plane boron atom vibrations. Therefore, the E_{2g} mode would take place simultaneously with, or include a strong coupling to, adjacent Mg atomic movements. For example, coupling with A_{1g} modes[1] is a reasonable expectation and may be evident in high resolution neutron diffraction investigations on $Mg_{1-x}Al_xB_2$ by Campi *et al.*[68] In Fig. 3 from this investigation,[68] it is shown that for no doping ($x = 0$), the radial distribution corresponding to the fourth periodicity in the *c*-direction is not four times the *c*-lattice parameter, in contrast to the first three periodicities (1, 2 and 3) which when divided by the respective multiples, all converge onto the same *c*-lattice parameter.

This work highlights the dynamic nature of structural symmetry when phonons are included. Phonons are equivalent to dynamical perturbations of the lattice oscillating at the frequency ω, as pointed out by d'Astuto *et al.*[2] As such, the phonon self-energy varies with time. To properly account for this, it is important to go beyond the adiabatic approximation to make use of time dependent perturbation theory.[2] According to Calandra *et al.*,[26] X-ray and Raman measurements are both explicable if dynamic effects beyond the adiabatic Born–Oppenheimer approximation as well as electron self-energy effects are included in the determination of phonon self-energy.

The use of reduced symmetry approximations as described in this study improves the description of phonon behaviour within the limitations of the adiabatic approximation. The potential JT-like PD that displays a "Mexican-hat" topology may be related to oscillatory electronic bands that are predicted to swing above and below the Fermi level as the lattice vibrates, with a corresponding charge population re-distribution when the band crosses the Fermi level.[69–71]

4.7 Phonon behaviour and superconductivity

The phenomenon of emergence and disappearance of Raman peaks as a function of temperature across the superconducting transition temperature, T_c, is indicative of a strong link to superconductivity.[10,15,19,24] The above discussion suggests that a peak at $\sim$116 cm^{-1} in Raman spectra may be attributed to a vibration mode in a lower symmetry structure. The energy of this peak at $\sim$116 cm^{-1} is approximately equal to the superconducting gap $2\Delta = 4k_BT_c$ ($\sim$111 cm^{-1}) for a $T_c \sim 40$ K, where k_B is Boltzmann's constant.

In this work, experimental data and computational models show that $\sim$230 cm^{-1} is an *A*-zone boundary frequency for the original *P*6/*mmm* unit cell (see Fig. 6 and 7). This frequency becomes part of the Γ-centre frequencies of the 2× super-lattice in the *c*-direction, following a procedure similar to that discussed by Kunc *et al.*[1] and shown in Fig. 9. Inspection of the *A*-zone boundary for the 2× super-lattice also shows that a frequency $\sim$116 cm^{-1} has been created at the new *A*-zone boundary (see Fig. 9). Therefore, an extension of the super-lattice symmetry to a 4× cell in the same direction as the 2× super-lattice results in a frequency value at the Γ-centre zone of 116 cm^{-1}. This analysis establishes a correlation between key phonon frequencies and a super-lattice with a commensurate modulation in the *c*-direction. Such a modulation

is likely to be of a dynamic nature and involve electron transfers to bonds and spin polarizations that define the super-lattice.

A fourfold modulation in the *c*-direction (*i.e.* a 4× super-lattice) corresponds to approximately 4 × 3.5 A = 14 A. This value is approximately half the coherence length for MgB_2 in the *c*-direction.[72,73] If we consider that the phonon anomaly minimum also corresponds to a super-lattice modulation in the *a*–*b* plane, we obtain approximately 7 × 3.08 A = 21.56 A, for the period of modulation. A factor of 7 times arises because the bottom of the anomaly is located at ~2 calculation points from the Γ-centre zone out of a total of 14 points that describe the direction to the *K*-zone boundary (see Fig. 6). A modulation in the *a*–*b* plane of ~22 A is approximately half the coherence length of about 44 A for MgB_2 in this direction.[72,73]

At the new zone boundary created by a super-lattice modulation in the *a*–*b* plane, extension of a line along the **k**-vector that corresponds to the minimum of the phonon anomaly determines the frequencies of the acoustic bands. This linear extension intersects the acoustic bands at frequencies ~50 cm^{-1}, ~75 cm^{-1} and ~120 cm^{-1}, respectively (see Fig. 9). These three frequencies have been detected in Raman investigations of MgB_2 with end values discussed in terms of pair breaking mechanisms and two superconducting gaps.[15,55]

4.8 Energy gaps and phonon relaxation

Tables 5 and 6 show that the following approximate balance of energies applies

$$A_{1g} (= B_{1g}) = E_{2g} + 116\ cm^{-1}$$

where B_{1g} and A_{1g} are the highest frequencies in Tables 5 and 6, (B_{1g} and A_{1g} ~ 710–715 cm^{-1}) and E_{2g} is ~600 cm^{-1}, respectively. B_{1g} and A_{1g} may convert with each other *via* accompanying charge movements that transforms group symmetry from *P6/mmm* to the lower symmetry double super-lattice. This equivalence provides not only a balance of energy, but an approximate mechanism where movements confined to the *a*–*b* plane may convert into movement in the *z*-direction leading to the creation of a switchable (on–off) dynamic super-lattice with corresponding boundary energy gaps.

An atom with three degrees of freedom has $k_BT/2$ thermal energy per degree of freedom.[74,75] Since MgB_2 has three atoms per unit cell, the thermal energy per unit cell of MgB_2 is $4.5k_BT$. At T_c, this thermal energy provides energy just above the superconducting gap $2\Delta = 4k_BT_c$, and thus, suggests that excitation of phonon modes that are separated by a gap energy is likely to be a significant determinant of superconductivity.

Fig. 11 shows a plot of the calculated frequencies for the 2× super-lattice using spectral values from Table 6, assuming integer multiples of the energy equivalent to the vibration mode of the lower symmetry structure noted in 4.7 above (*i.e.* ~116 cm^{-1}). These *ab initio* calculated frequencies define a linear trend based on the major acoustic mode for this super-lattice symmetry with other nearly parallel, slightly offset values. This trend suggests that the frequencies of the MgB_2 structure at the Γ-point have some similarity to those of an

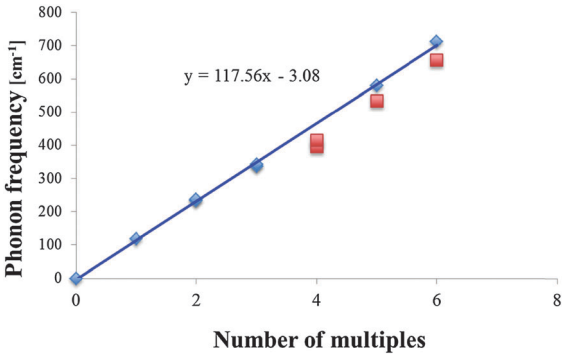

Fig. 11 *Ab initio* calculated frequencies at the Γ centre point derived from Table 6 compared as integer multiples of an energy value (~116 cm^{-1}) that correspond to the major acoustic energies for an MgB_2 super-lattice.

'harmonic oscillator', where the allowed frequencies are expressed as integer multiples of a basic value.[76–79]

Coherent phonon relaxation has been investigated in semiconductors[50,80] and is the basis for coherent phonon spectroscopy.[81] Coherent phonon relaxation is described in terms of phonon decay time and dephasing.[50,80,81] Decay times are typically longer at lower temperatures and dephasing may induce anharmonicity. Primary mechanisms in coherent phonon relaxation are up-conversion of modes by thermal phonons as well as down-conversion by decay of optical phonons into acoustic phonons.[50,80,81] In this latter case, acoustic phonons carry half the energy of the predecessor optical phonon but with opposing **k** vectors, thus conserving energy and momentum while avoiding incoherent scattering.

The linear integer proportionality of phonon frequencies at the Γ-point for MgB_2 noted above suggests that conversion of modes – where energy and momentum as well as phase coherence are conserved – is inferred from our combined experimental data and DFT calculations. For example, if the temperature cannot excite up-conversion from a particular energy level to the next higher energy mode, all remaining relaxation options are decay modes with phase coherent mechanisms.

This mechanism is exemplified by the available conversion processes from the important E_{2g} mode (~581 cm^{-1}). For example, when temperature remains above T_c, excitation into the 712 cm^{-1} mode is enabled by thermal phonons. Down-conversion from this higher level leads to scattering and resistive losses because decay paths with exclusively coherent options cannot be established. Once the temperature cannot excite up-conversion to the 712 cm^{-1} mode, the only remaining options for relaxation are decay modes within major phase coherent mechanisms.

Decay from the E_{2g} mode at ~581 cm^{-1} *via* two acoustic modes at ~116 cm^{-1} (with opposing momentum) lands at an energy level of 351 cm^{-1} which is observed in Raman spectra of MgB_2, (as shown in Table 2), and is also calculated for the 2× super-lattice (as shown in Table 6). The energy at 351 cm^{-1} belongs to the set of multiple integer values for MgB_2. Such a mechanism is not accessible for decay from the 712 cm^{-1}

mode, since two acoustic modes at $\sim$116 cm^{-1} do not land within available integer values. It is worth noting that the 351 cm^{-1} mode energy is approximately equivalent to half the B_{1g} and A_{1g} energy levels (at $\sim$712 cm^{-1}), which may also be important for energy conservation.

5. Conclusions

Combined Raman, IR and DFT investigations of high quality micrometer-sized MgB_2, allows a consistent explanation for experimentally-determined optical properties. Peaks in excess of those determined by group analysis of the *P*6/*mmm* symmetry have been detected using both Raman and IR spectroscopies. Some peaks display both Raman and IR activity, which indicates that the symmetry is reduced from *P*6/*mmm* to a non-centrosymmetric type.

PDOS calculations are insensitive to subtle changes in the PD produced by both commensurate and incommensurate super-lattice modulations. Similarly, frozen phonon approaches, which are limited to accurate determination of vibration frequencies at the Γ point, also mask crucial information at super-lattice positions. Computationally, the use of UPs appears to mask fine-scale charge re-distributions affecting the PD. Such charge re-distribution is associated with fluctuations of the nearly flat bands running parallel to the Fermi energy.[69–71]

DFT calculations of PDs and vibrational frequencies associated with a double cell in the *c*-direction explain the observed experimental data not only in this study but from several others which use different analytical techniques. PDs calculated with a 2$\times$ super-lattice produce a better overall shape and match to PDs determined from IXS and INS experimental data. Use of super-lattice symmetries for MgB_2 is a better-modelled approximation to dynamic modulations introduced by phonons.

Energy conservation through conversion of phonon energies by coherent relaxation may be manifest in the set of multiple integer frequencies reflected in the Raman and IR spectra of MgB_2 and may be a potential contributing mechanism for superconductivity in this material. This proposition is modelled using DFT and establishes a potential structural foundation for several key superconducting parameters. Extension of these concepts to other superconducting systems is currently in progress.

Acknowledgements

Financial assistance from QUT is gratefully acknowledged. Ongoing assistance with the high performance computing (HPC) facilities from Ashley Wright and Mark Barry, fruitful discussions with Professor John Barry, advice on Raman from Dr Llew Rintoul and assistance with sample preparation from Abigail Winnett are gratefully acknowledged.

References

1 K. Kunc, I. Loa, K. Syassen, R. K. Kremer and K. Ahn, *J. Phys.: Condens. Matter*, 2001, **13**, 9945–9962.
2 M. d'Astuto, M. Calandra, S. Reich, A. Shukla, M. Lazzeri, F. Mauri, J. Karpinski, N. D. Zhigadlo, A. Bossak and M. Krisch, *Phys. Rev. B: Condens. Matter Mater. Phys.*, 2007, **75**, 174508.
3 A. F. Goncharov and V. V. Struzhkin, *Phys. C*, 2003, **385**, 117–130.
4 A. F. Goncharov, V. V. Struzhkin, E. Gregoryanz, J. Hu, R. J. Hemley, H.-k. Mao, G. Lapertot, S. L. Bud'ko and P. C. Canfield, *Phys. Rev. B: Condens. Matter Mater. Phys.*, 2001, **64**, 10050(R).
5 J. Hlinka, I. G. J. Pokorný, A. Plecenik, P. Kúš, L. Satrapinsky and S. Beňačka, *Phys. Rev. B: Condens. Matter Mater. Phys.*, 2001, **64**, 140503(R).
6 L. Machtoub, Y. Takano and H. Kito, *Phys. C*, 2006, 445–448, 478–480.
7 H. Martinho, C. Rettori, P. G. Pagliuso, A. A. Martin, N. O. Moreno and J. L. Sarrao, *Solid State Commun.*, 2003, **125**, 499–502.
8 P. Postorino, A. Congeduti, P. Dore, A. Nucara, A. Bianconi, D. D. Castro, S. D. Negri and A. Saccone, *Phys. Rev. B: Condens. Matter Mater. Phys.*, 2001, **65**, 020507(R).
9 J. W. Quilty, S. Lee, A. Yamamoto, S. Tajima and A. Yamanaka, *Phys. C*, 2003, **388–389**, 131–132.
10 J. W. Quilty, *Phys. C*, 2003, **385**, 264–272.
11 P. M. Rafailov, S. Bahrs and C. Thomsen, *Phys. Status Solidi*, 2001, **226**, R9–R11.
12 P. M. Rafailov, M. Dworzak and C. Thomsen, *Solid State Commun.*, 2002, **122**, 455–458.
13 L. Shi, H. Zhang, L. Chen and Y. Feng, *J. Phys.: Condens. Matter*, 2004, **16**, 6541–6550.
14 K. A. Yates, G. Burnell, Z. Lockman, A. Kursumovic, J. L. M. Driscoll and M. G. Blamire, *J. Phys. Chem. Solids*, 2006, **67**, 333–335.
15 X. K. Chen, M. J. Konstantinović, J. C. Irwin, D. D. Lawrie and J. P. Franck, *Phys. Rev. Lett.*, 2001, **87**, 157002.
16 C. S. Sundar, A. Bharathi, M. Premila, T. N. Sairam, S. Kalavathi, G. L. N. Reddy, V. S. Sastry, Y. Hariharan and T. S. Radhakrishnan, Infrared absorption in superconducting MgB_2, 2001, arxiv.org/pdf/cond-mat/0104354.
17 A. Bharati, Y. Hariharan, J. Balaselvi and C. S. Sundar, *Sadhana*, 2003, **28**, 263–272.
18 A. Q. R. Baron, H. Uchiyama, S. Tsutsui, Y. Tanaka, D. Ishikawa, J. P. Sutter, S. Lee, S. Tajima, R. Heid and K.-P. Bohnen, *Phys. C*, 2007, **456**, 83–91.
19 A. Q. R. Baron, H. Uchiyama, Y. Tanaka, S. Tsutsui, D. Ishikawa, S. Lee, R. Heid, K.-P. Bohnen, S. Tajima and T. Ishikawa, *Phys. Rev. Lett.*, 2004, **92**, 197004.
20 A. Q. R. Baron, H. Uchiyama, R. Heid, K. P. Bohnen, Y. Tanaka, S. Tsutsui, D. Ishikawa, S. Lee and S. Tajima, *Phys. Rev. B: Condens. Matter Mater. Phys.*, 2007, **75**, 020505(R).
21 R. Osborn, E. A. Goremychkin, A. I. Kolesnikov and D. G. Hinks, *Phys. Rev. Lett.*, 2001, **87**, 017005.
22 T. Yildirim, O. Gülseren, J. W. Lynn, C. M. Brown, T. J. Udovic, Q. Huang, N. Rogado, K. A. Regan, M. A. Hayward, J. S. Slusky, T. He, M. K. Haas, P. Khalifah, K. Inumaru and R. J. Cava, *Phys. Rev. Lett.*, 2001, **87**, 037001.

23 N. D. Markovskiy, J. A. Mũnoz, M. S. Lucas, C. W. Li, O. Delaire, M. B. Stone, L. Abernathy and B. Fultz, *Phys. Rev. B: Condens. Matter Mater. Phys.*, 2011, **83**, 174301.
24 S. Tajima, T. Masui, J. Quilty, S. Lee, A. Yamamoto and A. Yamanaka, *Phys. C*, 2003, **388–389**, 103–104.
25 A. Y. Liu, I. I. Mazin and J. Kortus, *Phys. Rev. Lett.*, 2001, **87**, 087005.
26 M. Calandra, M. Lazzeri and F. Mauri, *Phys. C*, 2007, **456**, 38–44.
27 R. F. Wood, B. E. Sernelius and A. L. Chernyshev, *Phys. Rev. B: Condens. Matter Mater. Phys.*, 2002, **66**, 014513.
28 I. D. R. Mackinnon, A. Winnett, J. A. Alarco and P. C. Talbot, *Materials*, 2014, **7**, 3901–3918.
29 J. Nagamatsu, N. Nakagawa, T. Muranaka, Y. Zenitani and J. Akimitsu, *Nature*, 2001, **410**, 63–64.
30 J. D. Jorgensen, D. G. Hinks and S. Short, *Phys. Rev. B: Condens. Matter Mater. Phys.*, 2001, **63**, 224522.
31 S. Lee, H. Mori, T. Masui, Y. Eltsev, A. Yamamoto and S. Tajima, *J. Phys. Soc. Jpn.*, 2001, **70**, 2255–2258.
32 A. Shukla, M. Calandra, M. d'Astuto, M. Lazzeri, F. Mauri, C. Bellin, M. Krisch, J. Karpinski, S. M. Kazakov, J. Jun, D. Daghero and K. Parlinski, *Phys. Rev. Lett.*, 2003, **90**, 095506.
33 P. Dore, P. Postorino, A. Congeduti, A. Nucara, A. Bianconi, D. D. Castro, S. D. Negri and A. Saccone, *Int. J. Mod. Phys. B*, 2003, **17**, 505–511.
34 Y. Kong, O. V. Dolgov, O. Jepsen and O. K. Andersen, *Phys. Rev. B: Condens. Matter Mater. Phys.*, 2001, **64**, 020501(R).
35 K.-P. Bohnen, R. Heid and B. Renker, *Phys. Rev. Lett.*, 2001, **86**, 5771–5774.
36 K. Parlinski, *Ab Initio Study of Lattice Dynamics of MgB2*, IAEA/INIS, 2001.
37 ThermoScientific, GRAMS Spectrosocpy Software, http://www.thermoscientific.com/content/tfs/en/products/spectroscopy-software.html.
38 Accelrys, Materials Studio CASTEP Online Help: ''Predicting the thermodynamic properties of germanium'', http://www.tcm.phy.cam.ac.uk/castep/documentation/WebHelp/extfile/castep_tuts/html/castep_thermo_tut.htm#s4.
39 Accelrys, Materials Studio CASTEP Online Help: ''Requesting vibrational properties'', http://www.tcm.phy.cam.ac.uk/castep/documentation/WebHelp/html/tskcastepreqvibprops.htm.
40 J. A. Alarco, P. C. Talbot and I. D. R. Mackinnon, *Model. Numer. Simul. Mater. Sci.*, 2014, **4**, 53–69.
41 J. Zuo, C. Xu, Y. Liu and Y. Qian, *Nanostruct. Mater.*, 1998, **10**, 1331–1335.
42 G. Gouadec and P. Colomban, *Prog. Cryst. Growth Charact. Mater.*, 2007, **53**, 1–56.
43 O. Yassin, S. Alamri and A. Joraid, *J. Phys. D: Appl. Phys.*, 2013, **46**, 235301.
44 S. J. A. Pope and Y. D. West, *Spectrochim. Acta, Part A*, 1995, **51**, 2011–2017.
45 Y. D. West, *Internet J. Vib. Spectrosc.*, 1996, 1.
46 F. J. Deck, Rapid spatial averaging over an extended sample in a Raman spectrometer, *US Pat.*, US 7,595,873 B1, 2009.
47 F. Foucher, G. Lopez-Reyes, N. Bost, F. Rull-Perez, P. Rüßmann and F. Westall, *J. Raman Spectrosc.*, 2013, **44**, 916–925.
48 G. Ackland, M. Warren and S. Clark, *J. Phys.: Condens. Matter*, 1997, **9**, 7861.
49 B. Mihailova, presented in part at the Crystallography Online: International School on the Use and Applications of the Bilbao Crystallographic Server, Lekeitio, Spain, 2009.
50 M. Fox, *Optical Properties of Solids*, Oxford University Press, Reprint edn, 2003.
51 G. Turrell and J. Corset, *Raman Microscopy - Development and Applications*, Elsevier, Malta, 1996.
52 O. Tschauner, D. Errandonea and G. Serghiou, *Physica B*, 2006, **371**, 88–94.
53 T. Yildirim, http://www.ncnr.nist.gov/staff/taner/mgb2/.
54 M. Lazzeri, M. Calandra and F. Mauri, *Phys. Rev. B: Condens. Matter Mater. Phys.*, 2003, **68**, 220509(R).
55 G. Blumberg, A. Mialitsin, B. S. Dennis, N. D. Zhigadlo and J. Karpinski, *Phys. C*, 2007, **456**, 75–82.
56 S. Y. Savrasov, *Phys. Rev. B: Condens. Matter Mater. Phys.*, 1996, **54**, 16470–16486.
57 S. Y. Savrasov and D. Y. Savrasov, *Phys. Rev. B: Condens. Matter Mater. Phys.*, 1996, **54**, 16487–16501.
58 P. M. A. Sherwood, *Vibrational Spectroscopy of Solids*, Cambridge University Press, 1972.
59 J. M. Carlsson, Pseudopotentials: From Ultrahard to Ultrasoft, http://www.tcm.phy.cam.ac.uk/castep/CASTEP_talks_07/carlsson2.pdf.
60 D. R. Hamann, M. Schluter and C. Chiang, *Phys. Rev. Lett.*, 1979, **43**, 1494–1497.
61 R. Englman, *The Jahn–Teller Effect in Molecules and Crystals*, Wiley-Interscience, 1972.
62 G. A. Gehring and K. A. Gehring, *Rep. Prog. Phys.*, 1975, **38**, 1–89.
63 I. B. Bersuker, *The Jahn-Teller Effect*, Cambridge University Press, 2006.
64 I. B. Bersuker, *Electronic Structure and Properties of Transition Metal Compounds: Introduction to the Theory*, John Wiley & Sons Inc., 2nd edn, 2010.
65 P. B. Allen, in *Dynamical Properties of Solids*, ed. G. K. Horton and A. A. Maradudin, North Holland Publishing Company, 1980, ch. 2, vol. 3.
66 A. Q. R. Baron and H. Uchiyama, Kohn Anomaly in MgB2 and Related Compounds by Inelastic X-ray Scattering, http://www.spring8.or.jp/pdf/en/res_fro/03/054-055.pdf.
67 W. Kohn, *Phys. Rev. Lett.*, 1959, **2**, 393–394.
68 G. Campi, A. Ricci and A. Bianconi, *J. Supercond. Novel Magn.*, 2012, **25**, 1319–1322.
69 J. Kortus, I. I. Mazin, K. D. Belashchenko, V. P. Antropov and L. L. Boyer, *Phys. Rev. Lett.*, 2001, **86**, 4656–4659.
70 J. M. An and W. E. Pickett, *Phys. Rev. Lett.*, 2001, **86**, 4366–4369.
71 J. Kortus, http://www.physik.tu-freiberg.de/~kortus/kortus-research.html.
72 C. Buzea and T. Yamashita, *Supercond. Sci. Technol.*, 2001, **14**, R115–R146.

73 A. Narlikar, *Superconducting Magnesium Diboride*, NOVA Science Publishers Inc., 2002.
74 M. Baus and C. F. Tejero, *Equilibrium statistical physics: phases of matter and phase transitions*, Springer, 2007.
75 R. J. Hardy and C. Binek, *Thermodynamics and Statistical Mechanics: An Integrated Approach*, John Wiley & Sons, 2014.
76 C. Cohen-Tannoudji, B. Diu, F. Laloë, *Quantum Mechanics*, Hermann and John Wiley and Sons Inc., Paris, 1977, vol. 1.
77 L. D. Landau and E. M. Lifshitz, *Course of theoretical physics*, Elsevier, 1980.
78 A. Messiah, *Quantum Mechanics (Vol. I), English translation from French by GM Temmer*, North Holland, John Wiley & Sons, 1966.
79 M. Born and K. Huang, *Dynamical Theory of Crystal Lattices Oxford Classic Texts in the Physical Sciences*, Clarendon Press, Oxford, 1988.
80 F. Vallee, *Phys. Rev. B: Condens. Matter Mater. Phys.*, 1994, **49**, 2460.
81 T. Kohmoto, K. Tada, T. Moriyasu and Y. Fukuda, *Phys. Rev. B: Condens. Matter Mater. Phys.*, 2006, **74**, 1–5.